Experimental Protocols for The Assessment of Redox Thermodynamics of Nonstoichiometric Oxides: A Case Study of $YMnO_{3-\delta}$

Xin Qian,[1] Timothy C. Davenport,[1,4] Emanuela Mastronardo,[1,5] Sossina M. Haile[1,2,3]

[1]Department of Materials Science and Engineering, Northwestern University, Evanston, IL 60208, United States

[2]Program of Applied Physics, Northwestern University, Evanston, IL 60208, United States

[3]Department of Chemistry, Northwestern University, Evanston, IL 60208, United States

[4]Raytheon Technologies Research Center, East Hartford, CT 06074, United States

[5]Engineering Department, University of Messina, C.da di Dio, 98166, Messina, Italy

Correspondence

Sossina M. Haile, Walter P. Murphy Professor of Materials Science and Engineering, Northwestern University, Evanston, IL 60208, United States

Email: sossina.haile@northwestern.edu

ABSTRACT

The thermodynamics of reduction in variable valence oxides is important in a vast number of fields in which point defects, and in particular oxygen vacancies, control material functionality. Here we present, by way of an example measurement of the material $YMnO_{3-\delta}$, for which the vacancy formation energy has not been previously reported, best practices for material characterization. Sample mass is recorded by thermogravimetric analysis at temperatures from 600 to 1500 °C under five different gas atmospheres, with oxygen partial pressure ranging from 0.081 to 7.66×10^{-5} atm. Because $YMnO_{3-\delta}$, displays relatively small nonstoichiometry, less than 0.09, over the range of conditions examined, a large sample was required to record the modest mass changes. In the more oxidizing conditions equilibrium behavior was recorded using a finite heating rate of 10 °C min^{-1}. In the more reducing conditions, absolute mass changes with temperature were large such that the evolved oxygen increased the oxygen partial pressure in the sample vicinity, precluding equilibration under finite heating. Accordingly, a temperature-stepped protocol with long isothermal holds was employed. Analysis of the results from these stepped measurements required interpolation, which was carried out on the ln(™) vs $1/T$ plane. In the non-polar, centrosymmetric phase ($P6_3/mcm$ and ™ ε 0.016), the enthalpy of reduction was found to be 304 ± 4 kJ $(mol\text{-}O)^{-1}$, as averaged over the ™ range 0.020 to 0.035. While $YMnO_{3-\delta}$ is known to incorporate oxygen excess in its ambient temperature, polar phase ($P6_3cm$), the conditions leading to such behavior were not included in this study.

Keywords: nonstoichiometric oxides; perovskites; thermogravimetric analysis; measurement protocols; oxygen nonstoichiometry; thermodynamics of reduction

1. Introduction

Quantification of the thermodynamic properties of redox active oxides containing variable valence elements has been an active area of research for many years. Knowledge of such properties implies knowledge of defect concentration generated from changes in environmental conditions, specifically, temperature and oxygen chemical potential. The thermodynamics of oxide reduction are particularly relevant in the context of solar-driven thermochemical hydrogen (STCH) production, in which an oxide is thermally reduced at high temperature and subsequently oxidized using steam at low temperature, releasing hydrogen.[1, 2, 3] The thermodynamic properties dictate the maximum fuel that can be produced from a given thermochemical cycle, where the maximum corresponds to the case in which the material attains thermodynamic equilibrium by the conclusion of each step in the cycling process.[4, 5, 6] Less obvious is the fact that the rate of fuel production in many cases is also dictated by the thermodynamic properties of the oxide.[7, 8, 9] Oxide redox thermodynamics are similarly important in the context of thermal energy storage, in which the endothermic reduction step is performed when excess energy is available and subsequent oxidation releases energy when required.[10, 11] The defect chemistry of oxides moreover underpins the behavior of mixed ionic-electronic conductors used in the electrodes of solid oxide fuel cells, in which point defects generated by oxidation or reduction reactions control the rate of surface reactions as well as transport to and from reaction sites.[12]

Perhaps the most prevalent method for measuring the reduction properties of variable valence oxides is thermogravimetric analysis. Here one records the equilibrium mass of the material of interest under well-controlled conditions of temperature and oxygen partial pressure. While the method has been exploited with great success for many years, there are subtleties in both data collection and analysis that are easily overlooked. Here we describe recommended procedures for ensuring accuracy in such measurements, using $YMnO_{3-\delta}$ as the example. This oxide crystallizes in a hexagonal layered structure at

ambient temperature[13] (space group $P6_3cm$, isostructural to $LuMnO_{3-\delta}$) and has attracted interest due to its multiferroic behavior – it is ferrielectric at ambient conditions[13] - and due to its oxygen storage capacity – it incorporates oxygen excess into its structure upon exposure to oxygen at near-ambient temperatures.[14] At elevated temperatures, $YMnO_{3-\delta}$ displays a relatively small oxygen nonstoichiometry, δ, even under moderately reducing conditions. Hence, a study of $YMnO_{3-\delta}$ is useful for representing the steps required for characterizing a wide range of materials, both ones that are easy to reduce, with large mass changes, and those that are difficult to reduce, with small mass changes. The steps described here encompass: (1) chemical solution synthesis to ensure chemical and phase homogeneity; (2) preparation of self-supporting, porous monoliths for use in thermogravimetric analysis, structures which ensure gas access throughout measurement; (3) Y:Mn cation ratio measurement by several methods, which is essential for determining the absolute oxygen nonstoichiometry; (4) evaluation of thermal stability; and (5) measurement of equilibrium oxygen content by thermogravimetric analysis (TGA), where these data are then used to determine the thermodynamic properties. For experimental convenience, only the regime of oxygen deficiency is considered.

2. Methods

2.1 Materials Synthesis

The $YMnO_3$ of this work was synthesized via a chemical solution route[15] in which metal nitrates serve as the precursors for the metal species, ethylenediaminetetraacetic acid (EDTA) and citric acid serve as chelating agents, and ammonium hydroxide is used to adjust the pH and ensure solubility of the components. Reagents were $Y(NO_3)_3 \cdot 6H_2O$ (99.8% trace metal basis, Sigma Aldrich), $Mn(NO_3)_2 \cdot 4H_2O$ (≥ 97.5%, Acros Organics), EDTA (ACS 99.4+% Powder, Alfa Aesar), citric acid (ACS reagent, ≥ 99.5%, Sigma Aldrich), and ammonium hydroxide solution (ACS

reagent, 28.0 – 30.0% NH_3 basis, Sigma Aldrich), which were used without further purification. The reagent quantities were selected such that the molar ratio of EDTA to citric acid to the sum of the cations in the final solution was 1.5:1.5:1.

In the first step of the synthesis, stoichiometric amounts of the nitrates were dissolved in ~200 mL deionized water under magnetic stirring on a hot plate set at 40 °C. The EDTA was separately dissolved in ~50 mL ammonium hydroxide, which was then added to the fully dissolved nitrate solution under stirring. When precipitates appeared, more ammonia was added to bring the pH value to around 9 and induce precipitate dissolution. The citric acid was then added to the solution and, following its complete dissolution, more ammonia was added to adjust the pH value to about 10. The hot plate temperature was then increased to 180 °C and the solution held at this condition for 12 h to induce complete evaporation of the water. At this stage, a hard brown gel was obtained, and the beaker containing the sample was placed in an oven for drying at 250 °C for 24 h. The resulting black fluffy powder was transferred to an alumina crucible for calcination at 900 °C for 10 h under still air. The product was crushed and ground in an agate mortar into a fine powder. In the final step, porous monoliths of $YMnO_3$ were obtained by mixing ~0.5 g of the powder with isopropanol (ACS reagent, ≥ 99.5%, Sigma- Aldrich), lightly pressing the slurry in a uniaxial die, and then sintering the self-supporting green body at 1100 °C for 5 h under still air. At the conclusion of sintering, the material was cooled to ambient temperature at ~3 °C min^{-1}. The product had a porosity of ~60%, as estimated from a measurement of sample mass and dimensions. The material was used in the as-prepared, porous, monolithic form for all subsequent analyses, except XRD, for which it was ground prior to measurement.

2.2 Phase Characterization

The porous microstructure was characterized by Field Emission Scanning Electron Microscopy (FESEM, Hitachi SU8030). As part of the SEM studies, qualitative chemical analysis and assessment of chemical uniformity were performed by Energy Dispersive X-ray Spectroscopy (EDS, Oxford AZtec X-max 80 SDD, 20 kV, 10 mA). Quantitative chemical analysis was performed by Inductively Coupled Plasma – Optical Emission Spectrometry (ICP-OES, iCAP7000 ThermoFisher Scientific). For this purpose, ~5 mg was digested in a solution of 5% aqua regia for 12 h at room temperature and was further heated in a water bath at 65 °C for 30 min.

Phase formation was assessed by X-ray diffraction measurements (XRD) performed using a Rigaku Ultima IV diffractometer and Cu Kα (λ = 0.1541 nm) radiation (40 kV, 44 mA), over the 2θ range of 10 − 120°, with a step size of 0.05° and scanning speed of 5° min^{-1}. Measurements were performed (i) on the as-prepared material, (ii) on the material subsequent to its use in the suite of TGA measurements of oxygen content, (iii) on the material after exposure to selected additional high temperature conditions, and (iv) on the products obtained from a complete reduction experiment in which the as-prepared $YMnO_{3-\delta}$ was transformed into a mixture of Y_2O_3 and MnO. Analysis of the reduction product provided an additional means of determining the Y:Mn cation ratio. Full details of the reduction procedure and analysis methodology are provided below. Diffraction patterns were analyzed using the whole pattern fitting (WPF) function implemented in the commercial software JADE from Materials Data, Inc (MDI). Crystallographic parameters were analyzed by Rietveld refinement using the GSAS-II Crystallography Data Analysis Software.[16]

2.3 Thermogravimetric Analysis

It is relatively common in thermogravimetric studies to employ a stepped heating profile for the measurement of sample mass as a function of temperature because such a protocol enables easy recognition of when equilibrium has been attained. By waiting long enough at any given temperature, the

mass will stabilize towards a plateau value (assuming the absence of detrimental side reactions such has metal volatilization), which corresponds to the value that is sought. Such a procedure however limits the number of equilibrium data points that are recorded, which has downstream negative impacts on the extraction of thermodynamic parameters. The alternative protocol, in which one measures the mass continuously at finite heating rate, suffers from the possibility that the mass is not equilibrated over the course of the measurement, and worse, that the out-of-equilibrium behavior is not readily recognized. The benefit of the dynamic measurement, on the other hand, is the acquisition of the value of the mass at all temperatures, which can translate into more accurate determination of thermodynamic parameters. Notably, regardless of the heating protocol employed, sample mass is typically recorded in a TGA experiment continuously over time. Thus, even in a stepped heating protocol, mass changes that occur during the heating step are available. If equilibrium behavior can be demonstrated, these data can then provide the desired value of mass as a continuous function of temperature. Here we assess this behavior and provide guidance on optimal design of thermogravimetric experiments for the study of nonstoichiometric oxides.

Thermogravimetric data were collected under controlled gas atmospheres using a Netzsch STA449C simultaneous thermal analyzer, equipped with an oxygen partial pressure (pO_2) sensor (MicroPoas, Setnag) for off-gas analysis. Desired oxygen partial pressures were obtained by mixing Ar with one or more oxygen-poor gases, e.g., 10% O_2, 0.1% O_2, 10 ppm O_2 in Ar, or by using 'pure' Ar (certified by Air Liquide). To access strongly reducing conditions, a gas of 3% H_2 (balance Ar) was instead supplied. The gas flows were controlled by a series of digital mass flow controllers (MFCs), **Figure 1**(a), with the total flow rate fixed at 250 mL min^{-1}. The sensor was placed downstream of the TGA in a sealed quartz tube, in turn, placed in a furnace held at a temperature of 700 °C. The reported pO_2 values are those detected at the sensor. Preparation of the sample in the form of a pre-sintered, self-supporting porous

monolith, **Figure 1**(b), ensured gas access to the entirety of the material. To prevent possible reaction between the material and the alumina sample holder of the STA at high temperatures, the latter was covered by Pt foil prior to placement of the sample. Accurate detection of small relative mass changes was ensured by use of a large sample, ~1.73 g in total mass (comprising three of the fabricated monoliths). Given the instrument mass detection resolution of 0.1 μg, this large mass translates into a detection limit in δ of 6.9×10^{-7}. Instrument drift, however, as well as ambient laboratory noise, generally preclude measurements to such high accuracy. Nevertheless, even with a fluctuation in mass of ± 0.007 mg, as recorded in a typical isothermal hold, the uncertainty in δ is only 5×10^{-5}. Thus, factors such as precise temperature and gas composition control are more significant to accurate determination of thermodynamic properties than the precision of the mass measurement of a typical commercial thermogravimetric analysis instrument.

2.3.1 Oxygen Nonstoichiometry Profiles

Oxygen nonstoichiometry profiles were measured over the temperature range 600 to 1500 °C under five oxygen partial pressures: 0.081, 0.030, 4.35×10^{-4}, 1.95×10^{-4}, and 7.66×10^{-5} atm. Under the most oxidizing condition of pO_2 = 0.081 atm, the data collection was extended down to ambient temperature. For all measurements, the sample was equilibrated for 2 h at a reference state of T = 1000 °C and pO_2 = 0.081 atm prior to recording mass changes, and always returned to that state upon completion of the temperature cycle to confirm that mass changes were entirely due to reversible oxygen loss. Following the initial equilibration at the reference condition, the sample was cooled to 600 °C under the measurement gas of interest, and the temperature then raised in 100 °C increments at a heating rate of 10 °C min^{-1} between steps. Hence, all data in this work were collected using a nominally stepped heating profile, recognizing that mass loss is also recorded during the heating steps. Hold periods at the measurement temperatures ranged from 1 – 4 h, depending on the system requirements to reach, or at least

approach, equilibrium. Following the return to the reference condition, the sample was cooled in the reference gas and for this reason the low temperature behavior under pO_2 = 0.081 atm was also acquired. The same sample was used for all measurements. The sample was removed from the instrument following each pO_2 condition for the collection of the background (buoyancy) correction data, which are unique to each gas atmosphere. The pO_2 profile recorded over the course of the measurements was used for establishing equilibration.

2.3.2 Complete Reduction and Oxidation Analyses

The absolute oxygen content in the reference state was determined using a complete reduction procedure. Specifically, a sintered porous monolith, approximately 360 mg in mass was heated to the reference temperature (1000 °C) at a ramp rate of 5 °C min^{-1} and equilibrated under the reference gas (pO_2 = 0.081 atm, balance Ar) for 2 h. The system was then purged with Ar for 5 min. Following the purge, the sample was exposed to 3% H_2 (balance Ar) for 5 h, then cooled under the same gas atmosphere. The product was retrieved and ground for ex situ XRD analysis. The oxygen content in the reference state was further evaluated using the data collected under the reference gas (pO_2 = 0.081 atm), which was also the most oxidizing condition, upon cooling to ambient temperature.

3. Results and Discussion

3.1 Structure and Chemical Composition

The XRD Rietveld refinement analysis confirmed that single-phase, hexagonal $YMnO_3$ had been obtained, **Figure S1**(a) (Supplementary Materials), with lattice constants, a = 6.1485(3) Å and c =11.3999(6) Å, that agree with literature values. The SEM imaging, **Figure S1**(b) (Supplementary Materials), revealed the high porosity of the samples. The crystallite grains that make up the sample are no than ~500 nm in width, indicating relatively short solid-state diffusion lengths. The qualitative EDS

analysis of sintered $YMnO_3$ powder showed the Y:Mn ratio to be uniform across the sample. From the quantitative ICP-OES analysis the molar cation ratio was found to be Mn:Y = 1.003(2).

The complete reduction experiment, **Figure 2**(a), yielded Y_2O_3 (space group: Ia-3) and MnO (Fm-3m) as the reduction products, indicating that Mn was completely reduced to the 2+ oxidation state upon high temperature exposure to hydrogen. The Rietveld refinement, **Figure 2**(b), revealed lattice constants of a = 10.5939(2) Å for Y_2O_3 and a = 4.4535(2) Å for MnO. These values are within reasonable error of the reported values of the pure materials, 10.5981(7) Å[17] and 4.446(1) Å[18], respectively, indicating negligible (less than a fraction of a percent) solubility of MnO into Y_2O_3 and vice versa. The phase behavior of the MnO-Y_2O_3 system does not appear to have been reported in the literature. The observed mutual insolubility along with the refined Y_2O_3 phase fraction of 61.2(5) wt.% in the complete reduction product imply a molar cation ratio of Mn:Y = 1.007(8). Thus, both the direct chemical analysis and the phase analysis of the complete reduction product indicate that the material prepared here may be very slightly Y-deficient.

Though almost within the bounds of the experimental uncertainties, the slight deviation in Mn:Y ratio suggested from the chemical analysis has impact on the measurement of the absolute oxygen nonstoichiometry. Specifically, if the structure cannot accommodate cation interstitials, then the deviation in cation molar ratio implies vacancies on the cation-deficient sites. The material is accordingly described as $Y_{1-x}MnO_{3-\delta}$, and the stoichiometry $Y_{1-x}MnO_3$, in which all oxygen sites are fully occupied (δ = 0), corresponds to a state in which a small fraction, x, of the Mn ions are in the 4+ oxidation state. This state can be considered a pseudo-maximal oxidation state. Oxidation beyond this level is possible, but occurs under a distinct thermodynamic and crystal-chemical regime. For example, in $LaMnO_3$ (with a distorted perovskite structure), oxygen excess is associated with cation vacancies. In $YMnO_3$ oxygen incorporation into interstitial sites has been suggested, but this has been observed only at higher pO_2 than studied here.

Taking the cation off-stoichiometry into account, the complete reduction experiment, **Figure 2**(a), corresponds to the following (global) reaction

$$Y_{1-x}MnO_{3-\delta_0} \rightarrow 0.5(1-x)Y_2O_3 + MnO + (0.5-\delta_0)O_2$$

Using the ICP-OES determined value for x of 0.003 and noting the mass loss of 14.64 mg from the reference state mass of 358.580 ± 0.007 mg, δ_0 is found to be 0.012 ± 0.003. All subsequent thermogravimetric measurements were referenced to this value. It is of some note that the material is not in the pseudo-maximally oxidized state under the selected reference condition.

3.2 Thermogravimetric Measurement

Ex situ XRD of $YMnO_3$ indicated the absence of irreversible phase changes over the course of the TGA measurements of oxygen nonstoichiometry, **Figure S2** (Supplementary Materials), as required for interpretation of the mass loss in the context of the thermodynamics of reduction via oxygen nonstoichiometry. As reported above, the highest temperature and most reducing conditions of the TGA measurements were 1500 °C and $pO_2 = 7.66 \times 10^{-5}$ atm. Additional stability studies revealed the hexagonal phase was recovered even after exposure to 1550 °C under air, whereas exposure to 1600 °C (under air) induced melting, **Table S1** (Supplementary Materials).

Shown in **Figure 3** are the thermogravimetric profiles measured for $YMnO_3$ under the three more oxidizing conditions of this study: pO_2 = 0.081, 0.030, and 4.35×10^{-3} atm. Overall, as expected, the material loses mass upon heating and upon decreasing the gas phase oxygen partial pressure. Furthermore, the mass measured in the reference state at the initiation of the experiment is identical to that at the completion, consistent with mass changes due entirely to loss and uptake of oxygen. A significant feature of the data is the fixed mass across the isothermal holds. This is highlighted in the example profile shown in **Figure 3**(d) for a single heating step, in which it can be seen that the mass loss subsides immediately

upon reaching the new hold temperature. This result indicates that the mass is equilibrated at all temperatures throughout the heating step, despite the relatively rapid heating (10 °C min^{-1}). It can also be seen that the pO_2 is constant throughout the experiment. These factors indicate that the measurements have captured the equilibrium mass as a continuous function of temperature, despite the stepped heating protocol.

The TGA measurements under the two more reducing conditions of $pO_2 = 1.95 \times 10^{-4}$ and 7.66×10^{-5} atm, **Figure 4**, produced very different results from those of the more oxidizing conditions. Though the masses at the reference conditions at the initiation and the completion of the experiments were identical, indicating all mass changes are again due to reversible loss of oxygen, it is evident that the equilibrium mass was not attained for many of the isothermal hold conditions. This is particularly true at high temperatures, and for the more reducing of the two measurement conditions. Evident also in the data is the significant variation in pO_2 over the course of the measurements. During the heating step, the pO_2 increases beyond the inlet value. During the subsequent isothermal hold, it relaxes back, while the mass relaxes to a new (lower) value, as shown in detail for the 1300 → 1400 → 1500 °C steps under $pO_2 = 1.95 \times 10^{-4}$ atm, **Figure 4**(c). For the purpose of establishing equilibrium behavior under low pO_2, the profiles in the non-equilibrated isothermal regimes were evaluated by the procedure presented in **Figure 4**(d), in which the instantaneous oxygen nonstoichiometry is plotted as a function of the oxygen partial pressure detected at the sensor. At 1400 °C and lower, at both $pO_2 = 1.95 \times 10^{-4}$ and 7.66×10^{-5} atm, the gas composition relaxes back to the inlet value, or very close to it, and thus the final mass was taken to be the equilibrium value. At 1500 °C, even after two hours, the exhaust gas is rich in oxygen. An estimate for the equilibrium δ was obtained by extrapolation, but not used for further analysis. Ideally, the profiles shown in **Figure 4**(d) would represent equilibrium $\delta(pO_2)$ curves and would thus, for a given temperature, be aligned irrespective of the inlet pO_2. However, because of the long distance between the sample and the

sensor, and possible incomplete interaction of the sweep gas with the sample, the pO_2 recorded is not precisely that at the sample. Furthermore, the reduction is an endothermic process and the sample temperature, particularly at low pO_2, may be lower than the set temperature. These limitations are likely the reason for the offset between the $pO_2 = 1.95 \times 10^{-4}$ and 7.66×10^{-5} atm curves obtained at the same nominal temperature.

The oxygen non-stoichiometry data resulting from the TGA measurements are summarized in **Figure 5**. Both the data obtained during the isothermal holds, representing a typical stepped heating profile, and those obtained during the heating steps are shown. For the more oxidizing conditions (pO_2 = 0.081 atm – 4.35×10^{-3} atm), the data points representing the stepped profile are the averages over the 2 h holds, with uncertainties determined from the spread in the values. For the more reducing conditions ($pO_2 = 1.95 \times 10^{-4}$ atm, 7.66×10^{-5} atm), the discrete data points of the stepped profile are obtained by the extrapolation methods described above. Not surprisingly, the continuous $\delta(T)$ curves under more oxidizing conditions pass through the discrete points from the stepped analysis. This reflects the equilibrium behavior observed even under finite heating, **Figure 3**. In contrast, under the more reducing conditions, there is clear deviation in the data from the two approaches at high temperature. The out-of-equilibrium response under these conditions is a consequence of the large quantity of oxygen released for each increment of temperature under low pO_2, high temperature conditions. Material kinetic limitations, such as slow bulk diffusion or sluggish surface reaction, would *not* emerge as rate-limiting factors upon increasing temperature. Here, the use of a large mass of material ensures good resolution in the measurement of δ, but introduces a kinetic penalty because a large quantity of oxygen must be swept out of the system for equilibrium to be attained. In principle, this effect can be mitigated by increasing the gas flow rate, but was not pursued here due to the risk from possible buildup of pressure in the system and severe buoyancy effects.

Beyond the details of the comparison of measurement results, the results in **Figure 5** reveal somewhat unusual behavior in $YMnO_3$. Specifically, there is a surprising plateau in oxygen content at a δ of 0.016 that extends over the temperature range of approximately 700 to 1100 °C. Often, such a plateau reflects attainment of maximum oxidation. Here, however, the $\delta = 0$ condition is encountered at a lower temperature of ~ 250 °C under $pO_2 = 0.081$ atm. Furthermore, there is no evidence of oxygen excess in the structure over the conditions considered here, consistent with literature reports that indicate interstitial oxygen uptake only at higher oxygen partial pressures[14]. The possible association of this plateau with a phase transition is discussed below.

3.3 Thermodynamics of Reduction

Thermogravimetric data of the type presented in **Figure 5** reflect the thermodynamic properties of the material, which can be parameterized in terms of the enthalpy and entropy of reduction. The data treatment methods for extracting thermodynamic quantities have been described in the literature previously; the theory and steps are presented here for completeness. Under equilibrium conditions, the chemical potential of oxygen, μ_O, in the gas and solid phases in the TGA experiment are equal. By definition, the oxygen chemical potential is also the partial molar Gibbs energy of oxygen, $\bar{G}_O$. Taking oxygen in the gas phase to behavior as an ideal gas, a reasonable approximation for the pressures used in this study, the partial molar thermodynamic quantities of oxygen in the solid state are related to the oxygen pressure according to

$$\bar{G}_O(T) = \bar{H}_O - T\bar{S}_O = \mu_O^0(T) + RT\ln\left(\hat{p}_{O_2}^{1/2}\right)$$

where H is enthalpy, S is entropy, T is temperature, R is the universal gas constant, the superscript 0 indicates a value under standard pressure, and $\hat{p}_{O_2}$, the oxygen pressure relative to the reference pressure

(1 atm), is numerically equal to the partial pressure (pO_2). The relative partial molar quantities, i.e., relative to the standard state, are defined as

$$\mu_{\mathrm{O}}(T) - \mu_{\mathrm{O}}^{0}(T) = \Delta\bar{G}_{\mathrm{O}}^{0} = \Delta\bar{H}_{\mathrm{O}}^{0} - T\Delta\bar{S}_{\mathrm{O}}^{0} = RT\ln\left(\hat{p}_{\mathrm{O}_2}^{½}\right)$$

where each of the terms can and generally does depend on ™.

The relative partial molar Gibbs energy defined in Eq. is identical to the Gibbs energy of reaction for an infinitesimal extent of oxidation. Written with respect to reduction, the reaction for a generic ABO_3 compound is explicitly given as

$$\lim_{\Delta\delta\to 0}\left\{\frac{1}{\Delta\delta}\mathrm{ABO}_{3-\delta_{\mathrm{i}}} \rightarrow \frac{1}{\Delta\delta}\mathrm{ABO}_{3-\delta_{\mathrm{f}}} + \frac{1}{2}\mathrm{O}_2\right\}$$

with equilibrium constant $K_{red}^{eq} = \hat{p}_{\mathrm{O}_2}^{½}$, where $\Delta\delta = \delta_{\mathrm{f}} - \delta_{\mathrm{i}}$ is the change in oxygen non-stoichiometry between initial (δ_i) and final (δ_f) values. Rearranging Eq. and noting the relationship to the reduction reaction gives

$$\ln\left(\hat{p}_{\mathrm{O}_2}^{½}\right) = \frac{\Delta\bar{H}_{\mathrm{O}}^{0}}{RT} - \frac{\Delta\bar{S}_{\mathrm{O}}^{0}}{R} = \frac{-\Delta_{red}H^{0}}{RT} + \frac{\Delta_{red}S^{0}}{R}$$

Thus, a plot of oxygen partial vs temperature for an isostoichiometric condition in the Arrhenius representation (a van't Hoff plot[19, 20]) yields enthalpy as the slope and entropy as the intercept. If the plot is linear, as is frequently observed, then these thermodynamic terms are noted to be independent of temperature.

An alternative approach begins with a model of the point defect reaction that describes the reduction. The data are then interpreted in terms of the equilibrium constant for the prescribed reaction. In the present case, a reaction such as

$$2\mathrm{Mn}_{\mathrm{Mn}}^{\times} + \mathrm{O}_{\mathrm{O}}^{\times} \rightarrow 2\mathrm{Mn}_{\mathrm{Mn}}^{\prime} + \mathrm{V}_{\mathrm{O}}^{\bullet\bullet} + ½\mathrm{O}_2$$

might be considered, where defect species are indicated using Kroger-Vink notation.[21] While attractive because it limits the number of free parameters used to represent the thermodynamic data, this approach has the disadvantage of requiring *a priori* knowledge of the dominant defect reaction, the nature of which may change with extent of reduction. In the well-studied material, ceria, for example, the preponderance of the evidence indicates the presence of isolated Ce'_{Ce} defects at low reduction extent, whereas neutral trimer $(Ce'_{Ce}V_O^{\bullet\bullet}Ce'_{Ce})$ defects dominate at high reduction extent.[22, 23] Thus, a single formulation of the reduction reaction cannot describe all of the measured data. If the full suite of possible reactions are not explicitly treated, the point defect approach may bias the results towards a type of behavior that is not directly supported by the data.

Analysis of the thermogravimetric data by the reaction-agnostic global thermodynamic approach requires access to several T and pO_2 pairs corresponding to a given δ. In the case of the continuous nonstoichiometry profiles, δ is available at any value within the range of the measurements. One simply reads from the $\delta(T)$ profiles the set of temperatures which give rise to a specified, arbitrary δ. In the case of the stepped data, however, distinct values of δ are measured under different oxygen partial pressures, and the requisite isostoichiometric data are not immediately available. The question then becomes how to interpolate the data in a manner that minimizes the error introduced by doing so.

The interpolation procedure employed here (for estimating the temperature that yields a given δ at a given pO_2) derives from the relationship given in Eq. . Over a small range in δ, $\Delta_{red}H^0(\delta)$ can be treated as a constant. On the other hand, the entropy is typically a function of $R\ln(\delta)$. Thus, it is appropriate to consider entropy to be linear in $\ln(\delta)$ rather than δ, even over a small range. From these approximations one obtains

$$\ln(\delta) \propto \ln\left(\hat{p}_{O_2}^{½}\right) + \frac{\Delta_{red}\boldsymbol{H}^0}{RT}$$

where *H* in bold indicates a constant. This relationship implies that an Arrhenius plot of non-stoichiometry at a given pO_2 will be nearly linear. Thus, interpolation between measured δ and *T* points on an Arrhenius plot is physically justified and implies that the results are likely to be more accurate than those from linear interpolation between points in δ vs. *T*.

Shown in **Figure 6** is a summary of the data presented in the form of Arrhenius plots of the measured nonstoichiometry and of the isostoichiometric oxygen partial pressures. Here, the out-of-equilibrium heating segments from the low oxygen partial pressure conditions (1000 to 1400 °C) are omitted and are replaced with straight lines, while the measurements after even long holds at 1500 °C are also out of equilibrium and hence also omitted. The interpolation of nonstoichiometry in the Arrhenius form, **Figure 6**(a), along with the relatively small temperature steps in the stepped measurements, produces temperature values in the van't Hoff plot, **Figure 6**(b), that align well with those from the continuous measurements. Accordingly, the enthalpy and entropy of reduction functions extracted from these data, **Figure 7**, have very small errors from the linear van't Hoff fits. Alternative analysis approaches, that utilize only the continuous data, or use only the stepped data in conjunction with linear interpolations in δ-*T* plane, produce less satisfactory results, Figure S3 (Supplementary Materials).

The enthalpy and entropy functions, **Figure 7**, reflect the change in oxygen loss characteristics at $\delta \approx 0.016$ noted above. It has been reported that $YMnO_3$ undergoes a transition from the ambient-temperature polar, ferrielectric phase ($P6_3cm$) to a centrosymmetric structure ($P6_3/mcm$) at 985 °C (presumably under ambient atmosphere),[13] a temperature which coincides with that which $\delta \approx 0.016$ is encountered, 700 and 1100 °C, depending on pO_2. Thus, the sharp changes in $\Delta_{red}H^0(\delta)$ and $\Delta_{red}S^0(\delta)$ may reflect the transition from the ferrielectric to the centrosymmetric phase. The properties of the

centrosymmetric phase are measured here to greater reliability than those of the ferrielectric phase due to the greater reduction extent in the former. Nevertheless, a large difference between the thermodynamic properties of the two phases is clear, with the enthalpy rising by a factor of three and the entropy by a factor of two across the transition. Thus, thermogravimetric measurements can serve as a sensitive means of mapping phase behavior (as we have shown previously in the case of $CaMnO_3$[10]). Conversely, the high sensitivity to subtle changes in crystal structure suggest that structure tuning through chemical substitutions may emerge as a powerful means of controlling thermodynamic properties. Within the centrosymmetric phase, the enthalpy of reduction adopts an approximately δ-independent value of 304 ± 4 kJ $(mol\text{-}O)^{-1}$, as averaged over the δ range 0.020 to 0.035. Somewhat surprisingly, this value matches reasonably well atomistic level computational predictions of 335 kJ $(mol\text{-}O)^{-1}$ and 290 kJ $(mol\text{-}O)^{-1}$ made assuming a perovskite structure.[24, 25] Ignoring the unusual behavior of the ferrielectric phase, the large enthalpy of reduction can be attributed to the large energetic penalty of changing the Mn oxidation state from 3+ to 2+.[26] In the perovskite $LaMnO_3$, for example, the enthalpy of reduction is 350 kJ $(mol\text{-}O)^{-1}$,[27] similar to the value obtained here for $YMnO_3$. In compounds such as $CaMnO_3$, in which the reduction of Mn is from 4+ to a lower oxidation state, a lower enthalpy value has been measured, just 175 kJ $(mol\text{-}O)^{-1}$ in the slightly oxygen deficient cubic phase.[10] Compositional intermediates between the $LnMnO_3$ (Ln = lanthanide) and $AMnO_3$ (A = alkaline earth) generally result in intermediate values of enthalpy, particularly within the perovskite system,[27] and many such materials have been found to be more favorable for thermochemical fuel production than the end-members,[28] although some debate exists concerning doped $YMnO_{3-\delta}$.[29] In the present study of undoped $YMnO_{3-\delta}$, the apparent contradiction of strong sensitivity to crystal structure in regards to the difference between the ferrielectric and centrosymmetric phases in $YMnO_{3-\delta}$, but little sensitivity to structure between the centrosymmetric phase and a hypothetical perovskite form of $YMnO_{3-\delta}$ emerges as a surprising puzzle. Reconciling this contradiction will require

additional study, particularly in the low δ region.

4. Conclusions

Thermogravimetric measurements under well-controlled oxygen chemical potential provide access to the thermodynamics of reduction of variable valence oxides. As discussed in depth, measurements in which mass is recorded as a continuous function of temperature are preferable to those in which data are collected at stepped intervals because interpolations to determine the temperature and oxygen partial pressure conditions that give rise to specified values of nonstoichiometry are avoided. On the other hand, stepped measurements provide immediate information regarding equilibration of the system. Along with evidence of mass change with time under isothermal conditions, use of an in-line oxygen sensor allows detection of out-of-equilibrium behavior resulting from large amounts of oxygen release from the material during reduction, or conversely, large amounts of oxygen uptake during oxidation. Analysis of the results from the stepped measurements inherently requires interpolation. In such case, treatment of the data on the ln(™) vs $1/T$ plane is preferable to treatment on the ™ vs T plane.

The model material used for these studies, $YMnO_{3-\delta}$, displays relatively small nonstoichiometry, less than 0.09, over the range of conditions examined. Despite the modest mass changes, the thermodynamic properties have been recorded reliably through the procedures described here. In the non-polar centrosymmetric phase (™ ε 0.016), the enthalpy of reduction is 304 ± 4 kJ $(mol\text{-}O)^{-1}$, as averaged over the ™ range 0.020 to 0.035. While $YMnO_{3-\delta}$ is known to incorporate oxygen excess in the ambient temperature, polar phase, the conditions leading to such behavior were not examined in this work.

Conflict of interest

There are no conflicts to declare.

Acknowledgments

This research is funded by the US Department of Energy, through the office of Energy Efficiency and Renewable Energy (EERE) contract DE-EE0008089. The support from the European Union's Horizon 2020 research and innovation programme under the Marie Sklodowska-Curie grant agreement N° 746167 is also acknowledged. This work made use of the Jerome B. Cohen X-Ray Diffraction Facility supported by the MRSEC program of the National Science Foundation (DMR-1720139) at the Materials Research Center of Northwestern University and the Soft and Hybrid Nanotechnology Experimental (SHyNE) Resource (NSF ECCS-1542205).

References

1. W. C. Chueh, C. Falter, M. Abbott, D. Scipio, P. Furler, S. M. Haile, and A. Steinfeld, "High-flux solar-driven thermochemical dissociation of CO_2 and H_2O using nonstoichiometric ceria," *Science,* 330[6012] 1797-801 (2010).

2. M. Romero and A. Steinfeld, "Concentrating solar thermal power and thermochemical fuels," *Energy & Environmental Science,* 5[11] 9234-45 (2012).

3. B. Bulfin, J. Vieten, C. Agrafiotis, M. Roeb, and C. Sattler, "Applications and limitations of two step metal oxide thermochemical redox cycles; a review," *Journal of Materials Chemistry A,* 5[36] 18951-66 (2017).

4. W. C. Chueh and S. M. Haile, "A thermochemical study of ceria: exploiting an old material for new modes of energy conversion and CO_2 mitigation," *Philosophical Transactions of the Royal Society of London A: Mathematical, Physical and Engineering Sciences,* 368[1923] 3269-94 (2010).

5. B. Meredig and C. Wolverton, "First-principles thermodynamic framework for the evaluation of thermochemical H_2O-or CO_2-splitting materials," *Physical Review B,* 80[24] 245119 (2009).

6. J. Vieten, B. Bulfin, P. Huck, M. Horton, D. Guban, L. Zhu, Y. Lu, K. A. Persson, M. Roeb, and C. Sattler, "Materials design of perovskite solid solutions for thermochemical applications," *Energy & Environmental Science,* 12[4] 1369-84 (2019).

7. M. J. Ignatowich, A. H. Bork, T. C. Davenport, J. L. M. Rupp, C.-k. Yang, Y. Yamazaki, and S. M. Haile, "Impact of enhanced oxide reducibility on rates of solar-driven thermochemical fuel production," *MRS Communications,* 7[4] 873-78 (2017).

8. T. C. Davenport, C.-K. Yang, C. J. Kucharczyk, M. J. Ignatowich, and S. M. Haile, "Implications of exceptional material kinetics on thermochemical fuel production rates," *Energy Technology,* 4[6] 764-70 (2016).

9. T. C. Davenport, C.-K. Yang, C. J. Kucharczyk, M. J. Ignatowich, and S. M. Haile, "Maximizing fuel production rates in isothermal solar thermochemical fuel production," *Applied Energy,* 183 1098-111 (2016).

10. E. Mastronardo, X. Qian, J. M. Coronado, and S. M. Haile, "The favourable thermodynamic properties of Fe-doped $CaMnO_3$ for thermochemical heat storage," *Journal of Materials Chemistry A,* 8[17] 8503-17 (2020).

11. E. Mastronardo, X. Qian, J. M. Coronado, and S. M. Haile, "Impact of La doping on the thermochemical heat storage properties of $CaMnO_{3-\delta}$," *Journal of Energy Storage,* 40 102793 (2021).

12. N. H. Perry and T. Ishihara, "Roles of bulk and surface chemistry in the oxygen exchange kinetics and related properties of mixed conducting perovskite oxide electrodes," *Materials,* 9[10] 858 (2016).

13. A. S. Gibbs, K. S. Knight, and P. Lightfoot, "High-temperature phase transitions of hexagonal $YMnO_3$," *Physical Review B,* 83[9] 094111 (2011).

14. C. Abughayada, B. Dabrowski, S. Kolesnik, D. E. Brown, and O. Chmaissem, "Characterization of oxygen storage and structural properties of oxygen-loaded hexagonal $RMnO_{3+\delta}$ (R = Ho, Er, and Y)," *Chemistry of Materials,* 27[18] 6259-67 (2015).

15. Y. Yamazaki, R. Hernandez-Sanchez, and S. M. Haile, "High total proton conductivity in large-grained yttrium-doped barium zirconate," *Chemistry of Materials,* 21[13] 2755-62 (2009).

16. B. H. Toby and R. B. Von Dreele, "GSAS-II: the genesis of a modern open-source all purpose crystallography software package," *Journal of Applied Crystallography,* 46[2] 544-49 (2013).

17. E. N. Maslen, V. A. Streltsov, and N. Ishizawa, "A synchrotron X-ray study of the electron density in C-type rare earth oxides," *Acta Crystallographica Section B,* 52[3] 414-22 (1996).

18. S. Sasaki, K. Fujino, Tak, Eacute, and Y. Uchi, "X-ray determination of electron-density distributions in oxides, MgO, MnO, CoO, and NiO, and atomic scattering factors of their constituent atoms," *Proceedings of the Japan Academy, Series B,* 55[2] 43-48 (1979).

19. R. J. Panlener, R. N. Blumenthal, and J. E. Garnier, "A thermodynamic study of nonstoichiometric cerium dioxide," *Journal of Physics and Chemistry of Solids,* 36[11] 1213-22 (1975).

20. Y. Hao, C.-K. Yang, and S. M. Haile, "Ceria–zirconia solid solutions ($Ce_{1-x}Zr_xO_{2-\delta}$, $x \leq 0.2$) for solar thermochemical water splitting: a thermodynamic study," *Chemistry of Materials,* 26[20] 6073-82 (2014).

21. F. A. Kröger and H. J. Vink, "Relations between the concentrations of imperfections in solids," *Journal of Physics and Chemistry of Solids,* 5[3] 208-23 (1958).

22. R. Schmitt, A. Nenning, O. Kraynis, R. Korobko, A. I. Frenkel, I. Lubomirsky, S. M. Haile, and J. L. M. Rupp, "A review of defect structure and chemistry in ceria and its solid solutions," *Chemical Society Reviews,* 49[2] 554-92 (2020).

23. K. L. Duncan, Y. Wang, S. R. Bishop, F. Ebrahimi, and E. D. Wachsman, "The role of point defects in the physical properties of nonstoichiometric ceria," *Journal of Applied Physics,* 101[4] 044906 (2007).

24. A. A. Emery, J. E. Saal, S. Kirklin, V. I. Hegde, and C. Wolverton, "High-throughput computational screening of perovskites for thermochemical water splitting applications," *Chemistry of Materials,* 28[16] 5621-34 (2016).

25. M. Ezbiri, M. Takacs, B. Stolz, J. Lungthok, A. Steinfeld, and R. Michalsky, "Design principles of perovskites for solar-driven thermochemical splitting of CO_2," *Journal of Materials Chemistry A,* 5[29] 15105-15 (2017).

26. R. B. Wexler, G. S. Gautam, E. B. Stechel, and E. A. Carter, "Factors governing oxygen vacancy formation in oxide perovskites," *Journal of the American Chemical Society,* 143[33] 13212-27 (2021).

27. C.-K. Yang, Y. Yamazaki, A. Aydin, and S. M. Haile, "Thermodynamic and kinetic assessments of strontium-doped lanthanum manganite perovskites for two-step thermochemical water splitting," *Journal of Materials Chemistry A,* 2[33] 13612-23 (2014).

28. S. Dey, B. S. Naidu, A. Govindaraj, and C. N. R. Rao, "Noteworthy performance of $La_{1-x}Ca_xMnO_3$ perovskites in generating H_2 and CO by the thermochemical splitting of H_2O and CO_2," *Phys. Chem. Chem. Phys.,* 17[1] 122-25 (2015).

29. R. J. Carrillo, C. M. Hill, K. J. Warren, and J. R. Scheffe, "Oxygen nonstoichiometry and defect equilibria of yttrium manganite perovskites with strontium A-site and aluminum B-site doping," *J. Phys. Chem. C,* 124[8] 4448-58 (2020).

Figures

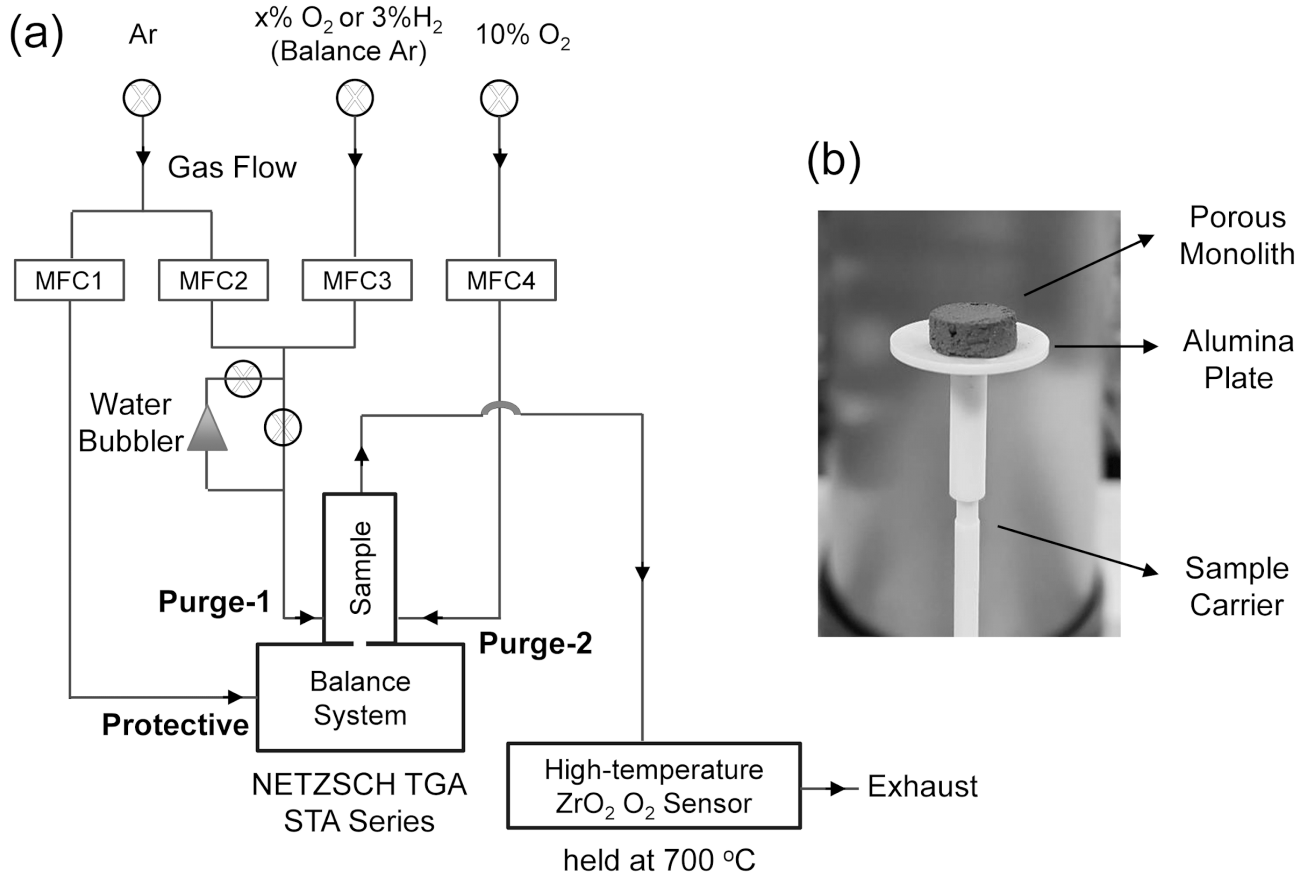

Figure 1. Experimental methods for thermogravimetric measurements: (a) schematic of the gas flow arrangement, providing access to a wide range of oxygen partial pressures, with gas composition confirmed using a downstream, in-line oxygen sensor; and (b) optical photograph of a representative sintered porous monolith placed on the alumina plate of the TGA sample carrier. Photograph reproduced from Mastronardo et al.[10] with permission from the Royal Society of Chemistry.

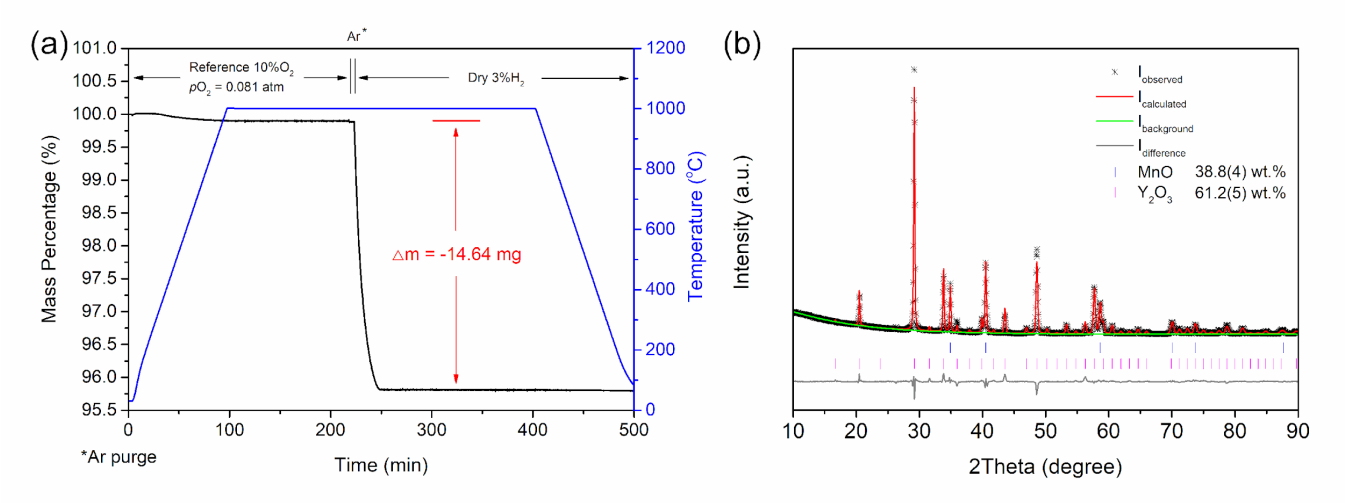

Figure 2. Complete reduction experiment of $YMnO_{3-\delta}$ by exposure to 3% H_2 (balance Ar) at 1000 °C using a sample mass of 358.94 mg: (a) mass and temperature profiles, and (b) XRD Rietveld refinement analysis of the reduced products.

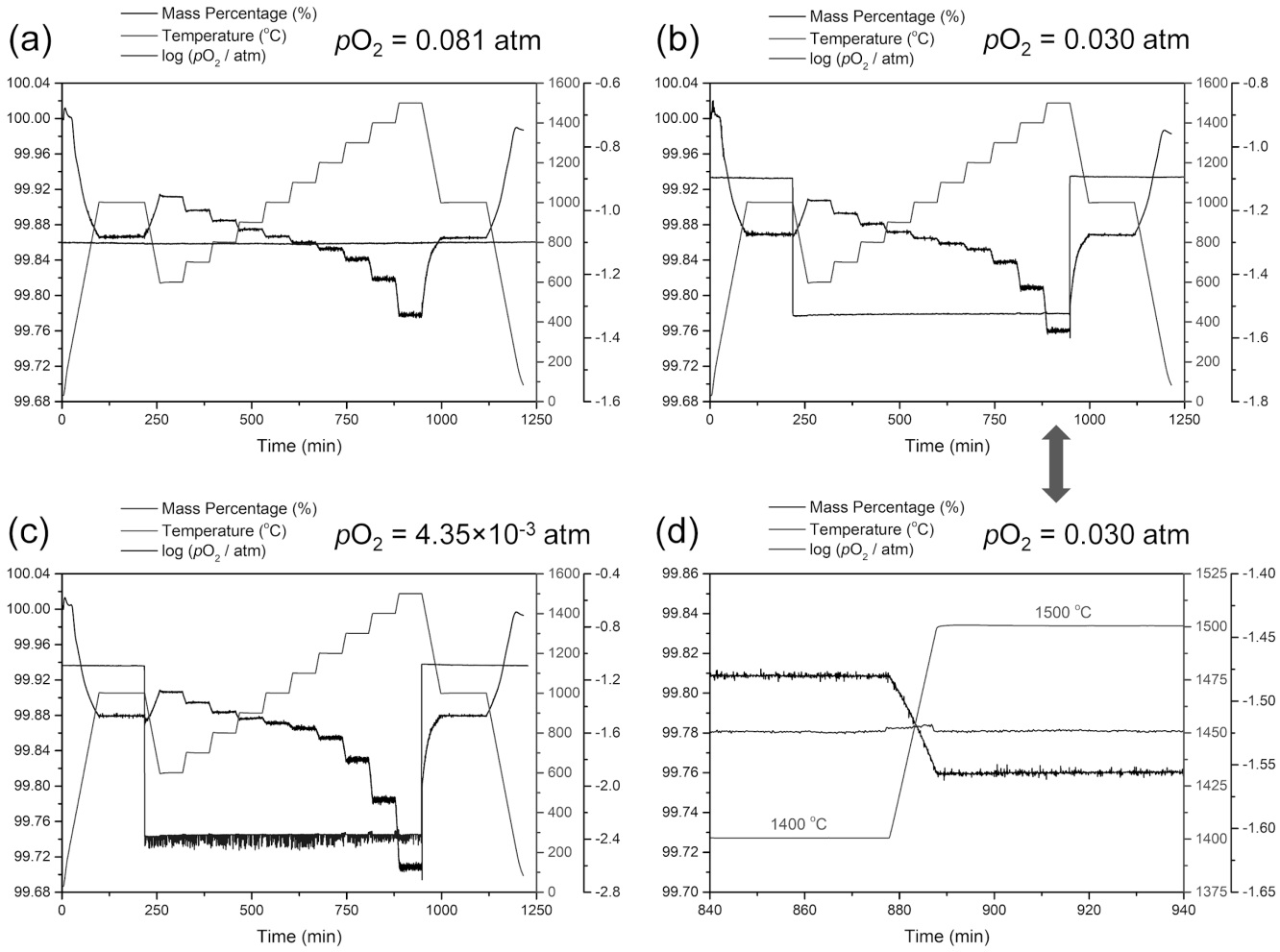

Figure 3. Mass, temperature, and pO_2 profiles of $YMnO_{3-\delta}$ under relatively oxidizing atmospheres using a stepped heating protocol: (a) pO_2 = 0.081 atm, m_0 = 1735.19 mg; (b) pO_2 = 0.030 atm, m_0 = 1732.00 mg; (c) $pO_2 = 4.35 \times 10^{-3}$ atm, m_0 = 1731.70 mg; (d) enlarged profiles between 1400 °C and 1500 °C from (b), showing equilibrated behavior during the heating period, with a heating rate of 10 °C min^{-1}.

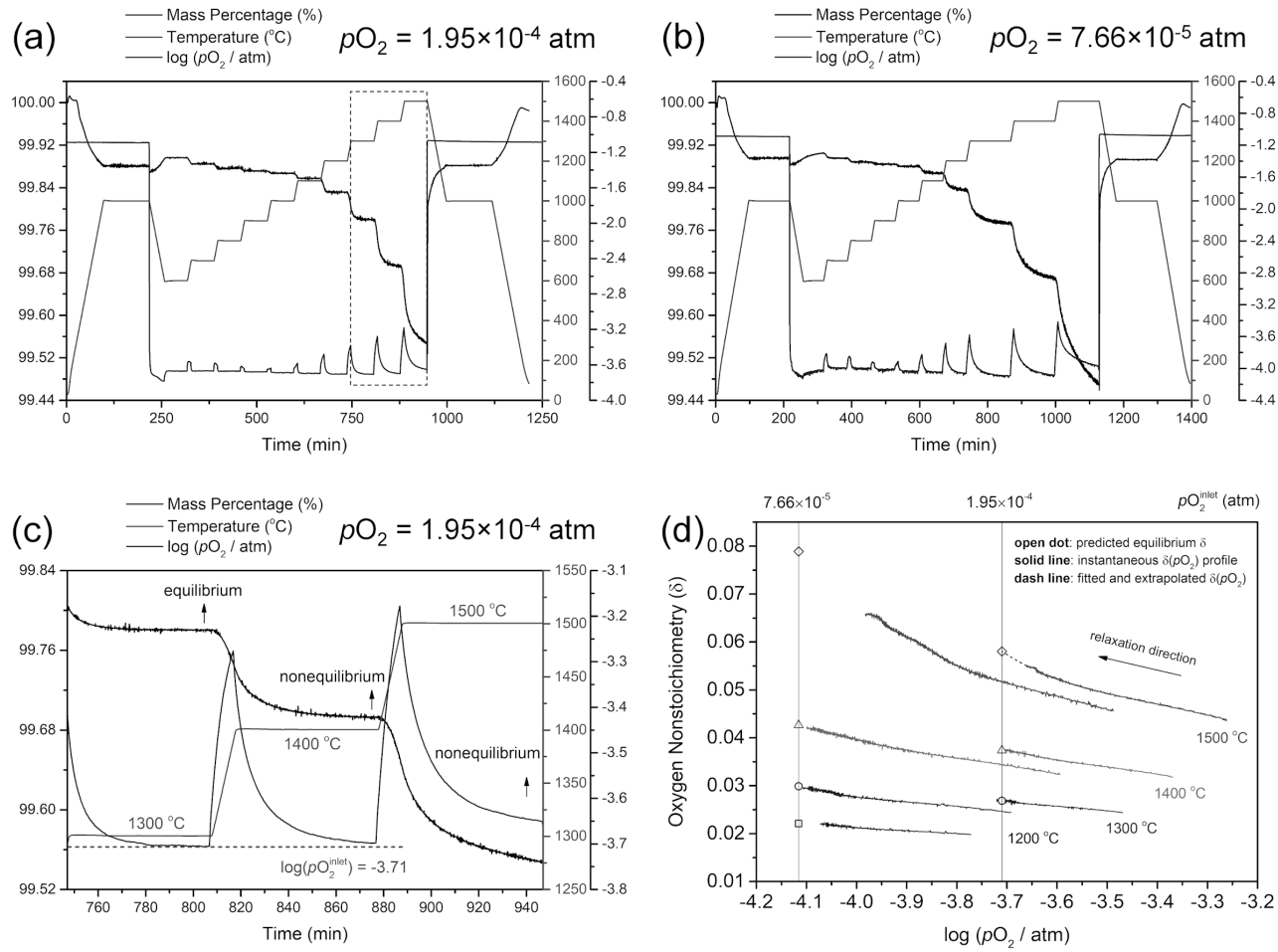

Figure 4. Mass, temperature, and pO_2 profiles of $YMnO_{3-\delta}$ under relatively reducing atmospheres using a stepped heating protocol: (a) $pO_2 = 1.95 \times 10^{-4}$ atm, $m_0 = 1731.30$ mg; (b) $pO_2 = 7.66 \times 10^{-5}$ atm, $m_0 = 1730.70$ mg; (c) enlarged profiles between 1300 and 1500 °C from (a), and (d) the oxygen nonstoichiometry during the isothermal relaxation period.

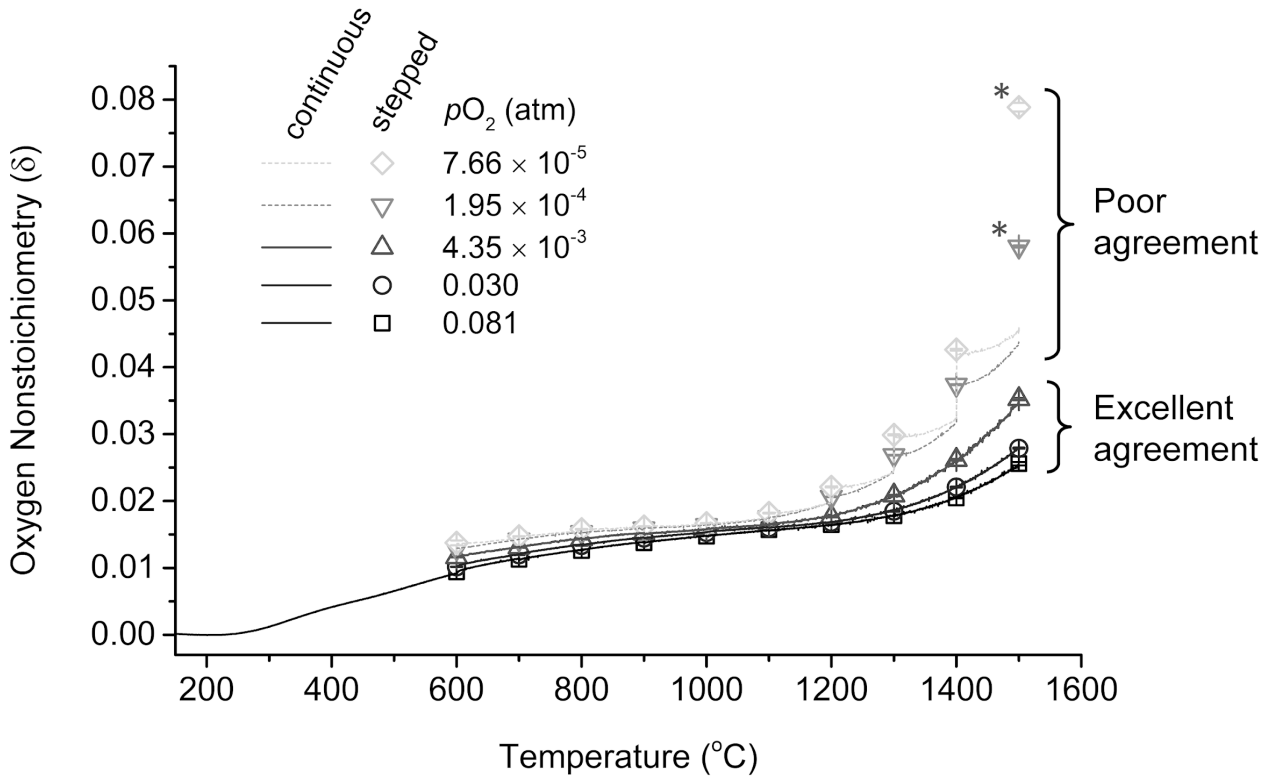

Figure 5. The absolute oxygen nonstoichiometry of $YMnO_{3-\delta}$. The continuous curves are obtained from the instantaneous δ(T) in the ramp between temperature steps whereas the symbols represent the values obtained during the hold periods, or upon extrapolation to equilibrium values during the hold. Datapoints marked with an asterisk omitted in subsequent thermodynamic analysis.

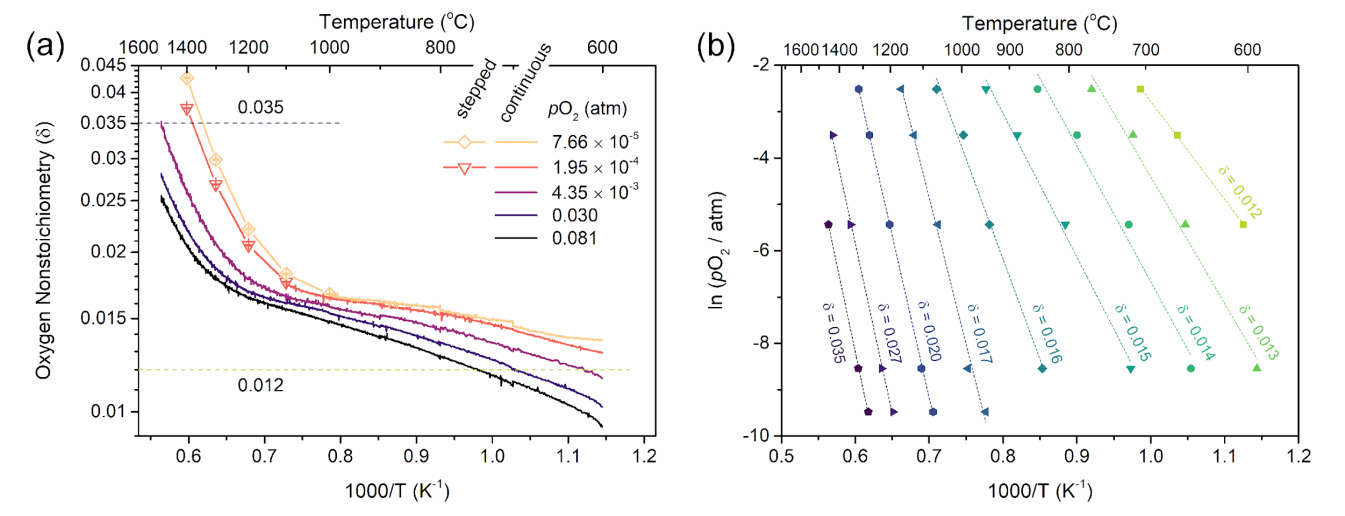

Figure 6. Arrhenius representations of the nonstoichiometry of $YMnO_{3-\delta}$: (a) nonstoichiometry as a function of temperature; and (b) isostoichiometric contours at selected δ for the determination of thermodynamic properties by the van't Hoff method, for all cases, $R^2 > 0.98$. In (a) line segments between data symbols are straight lines used for linear interpolation and do not reflect measured data. In (b) straight lines are linear fits to the plotted data points.

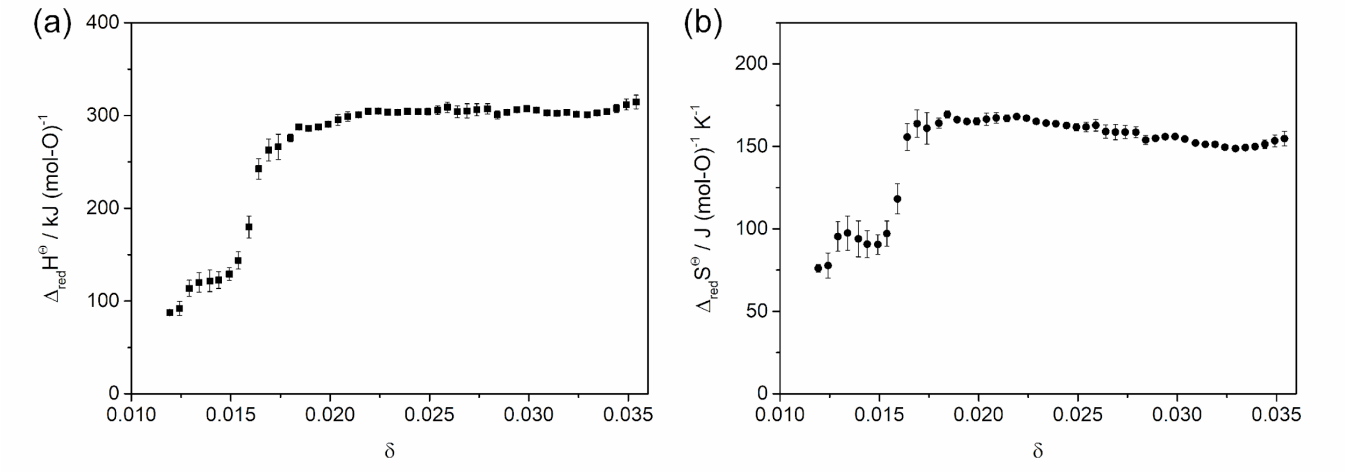

Figure 7. The thermodynamic properties of $YMnO_{3-\delta}$ determined using oxygen nonstoichiometry profiles in Figure 6: (a) standard enthalpy, and (b) standard entropy of reduction.

Supplementary Information

Experimental Protocols for The Assessment of Redox Thermodynamics of Nonstoichiometric Oxides: A Case Study of $YMnO_{3-\delta}$

Xin Qian,[1] Timothy C. Davenport,[1,4] Emanuela Mastronardo,[1,5] Sossina M. Haile[1,2,3]

[1]Department of Materials Science and Engineering, Northwestern University, Evanston, IL 60208, United States

[2]Program of Applied Physics, Northwestern University, Evanston, IL 60208, United States

[3]Department of Chemistry, Northwestern University, Evanston, IL 60208, United States

[4]Raytheon Technologies Research Center, East Hartford, CT 06074, United States

[5]Engineering Department, University of Messina, C.da di Dio, 98166, Messina, Italy

Correspondence

Sossina M. Haile, Walter P. Murphy Professor of Materials Science and Engineering, Northwestern University, Evanston, IL 60208, United States

Email: sossina.haile@northwestern.edu

Supplemental Figures

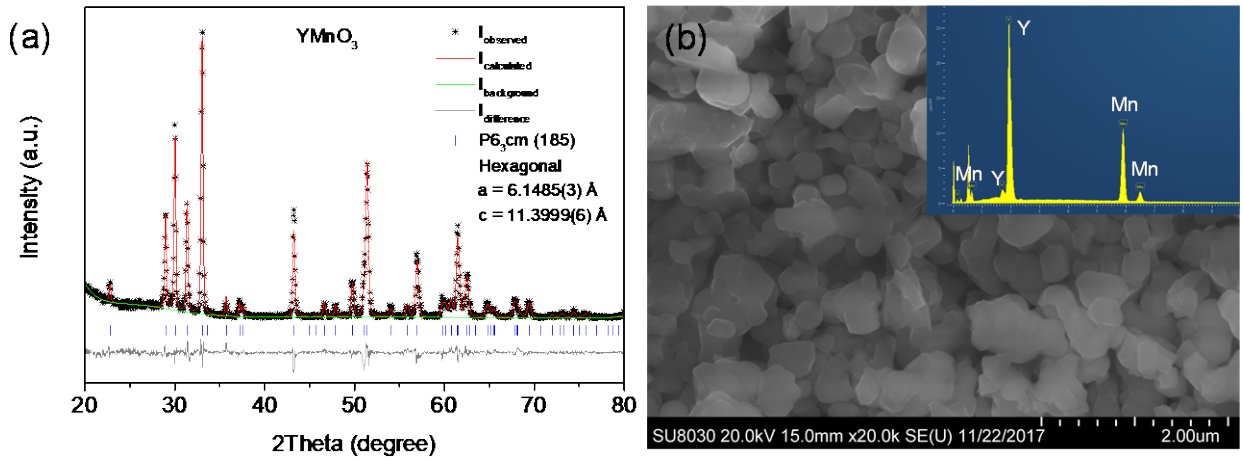

Figure S1. (a) Rietveld refinement analysis of the powder X-ray diffraction pattern of $YMnO_3$ after sintering at 1100 °C for 5h under air; (b) scanning electron microscopy top-view of the surface morphology of a sintered lightly pressed porous monolith, inset graph shows the collected EDS spectrum.

Based on the XRD Rietveld refinement analysis of $YMnO_3$ bulk powder, Figure S1(a), diffraction peaks were indexed to $YMnO_3$ with the hexagonal structure in the space group of $P6_3cm$ (185) (Powder Diffraction File (PDF) no. 04-011-9913, International Centre for Diffraction Data (ICDD), [2010]). Rietveld refinement of the diffraction pattern using GSAS-II crystallography data analysis software suggested that the as-prepared $YMnO_3$ was phase pure without impurities. Shown in Figure S1(b) was surface morphology of the porous structure of lightly pressed monolith, the high porosity (~60 %) provided open access for gases to react with the solid phase and the small particle size (~500 nm) enabled rapid solid-state diffusion of ionic species in the bulk. Chemical analysis by EDS, as shown in the inset graph in Figure S1(b), confirmed the elemental compositions of Y and Mn in the synthesized material $YMnO_3$ without other impurities.

Table S1. Exposure conditions for the evaluation of thermal stability of $YMnO_3$ by ex situ X-ray diffraction. Heat treatment under air was performed in tube furnace, whereas at that at lower pO_2 was performed in the TGA, the ramp rate for all treatments is 2 °C min^{-1}. The lattice constants of the annealed products are obtained by Rietveld refinement.

Anneal pO_2 (atm)	Temperatures (°C)	Hold Time (h)	Cooling pO_2 (atm)	Post-treatment Crystal Structure	Refined Lattice Constants (Å)
Air (0.21)	1400	1	Air (0.21)	Hexagonal	a = 6.1457(2) c = 11.3923(3)
Air (0.21)	1500	1	Air (0.21)	Hexagonal	a = 6.1456(1) c = 11.3938(4)
Air (0.21)	1550	1	Air (0.21)	Hexagonal	a = 6.1483(5) c = 11.3995(3)
Air (0.21)	1600	1	Air (0.21)	Melted	--
7.66×10^{-5}	1500	2	0.081	Hexagonal	a = 6.1423(3) c = 11.3965(4)
after exposure to all TGA measurement conditions				Hexagonal	a = 6.1441(2) c = 11.3993(1)

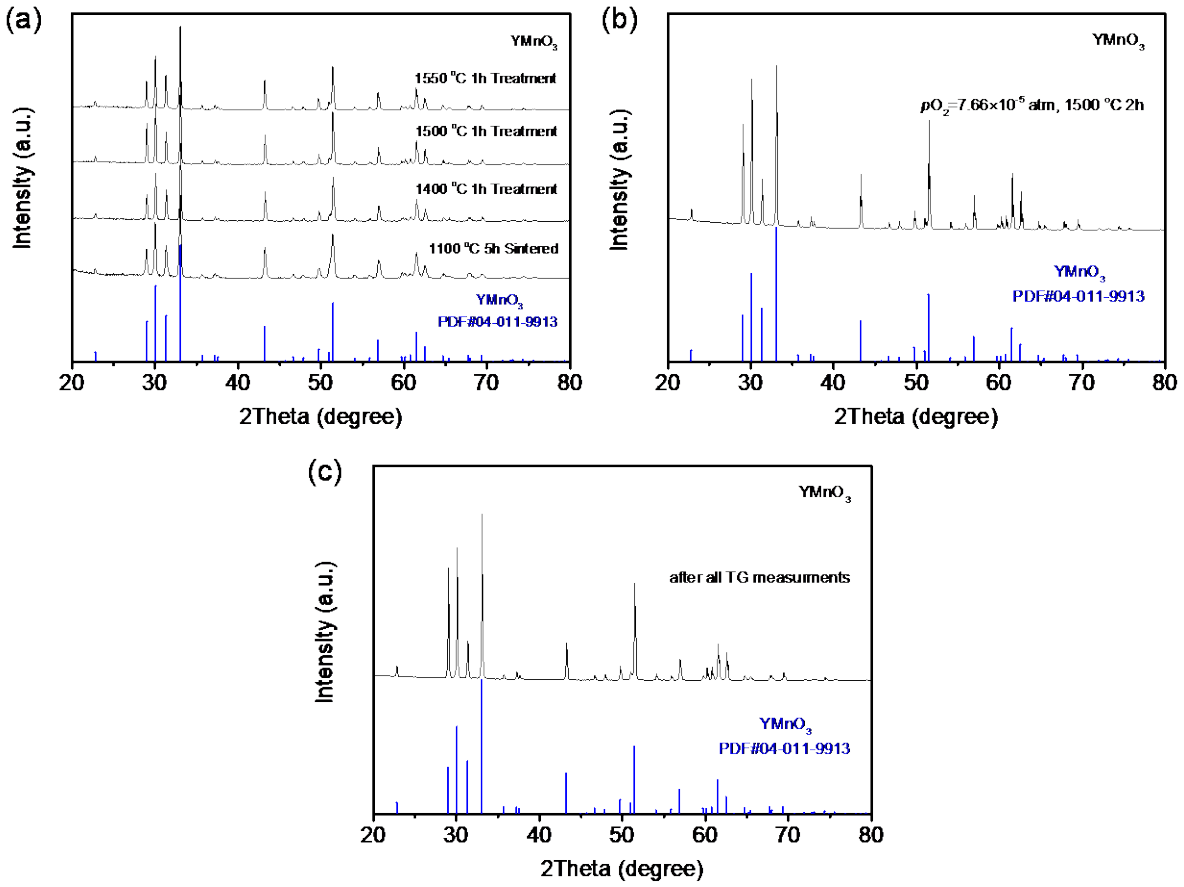

Figure S2. Ex situ X-ray powder diffraction patterns collected on $YMnO_3$ after exposure of the sintered porous pellets to various conditions indicated: (a) pO_2 = 0.21 atm (air), at temperatures of 1400 °C, 1500 °C, 1550 °C and 1600 °C for 1h, the sample was melted after exposure to 1600 °C in air; (b) $pO_2 = 7.66 \times 10^{-5}$ atm, at 1500 °C for 2h; (c) after exposure to all thermogravimetric measurement conditions indicated in Figures 3 and 4.

After exposure to various high temperature and oxygen partial pressure conditions, ex situ XRD characterizations revealed that $YMnO_3$ was stable up to 1550 °C under air and up to at least 1500 °C under $pO_2 = 7.66 \times 10^{-5}$ atm, Figure S2(a,b), which allowed thermogravimetric measurements to be carried out in the temperature range from 600 to 1500 °C under an oxygen partial pressure as low as $pO_2 = 7.66 \times 10^{-5}$ atm. Shown in Figure S2(c) was the diffraction pattern collected on the sample after all thermogravimetric measurements displayed in Figures 3 and 4, from which the

material was confirmed to remain in a single-phase hexagonal crystal structure, providing further confidence in the measured thermodynamics properties. The lattice constants of annealed $YMnO_3$ resulting from XRD Rietveld refinement analyses after each heat treatment were summarized in Table S1.

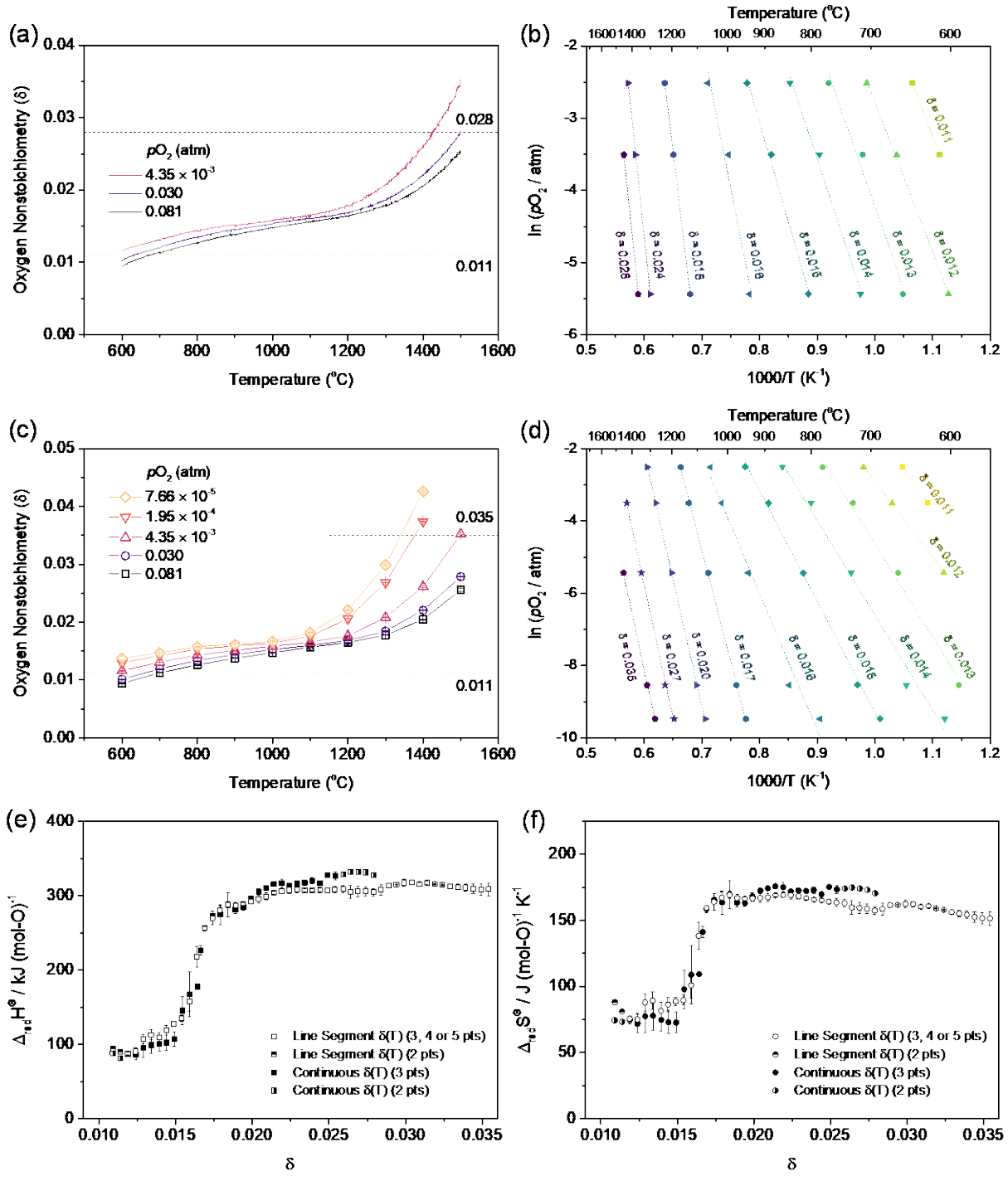

Figure S3. Oxygen nonstoichiometry of $YMnO_{3-\delta}$: (a) summary of the continuous δ(T) results of Figures 3, and (b) Arrhenius representation for the extraction of thermodynamic properties by the van't Hoff method at selected fixed δ between 0.011 and 0.028 using the data obtained from the

continuous δ(T) profiles; (c) summary of the stepped δ used for extracting the thermodynamic properties (data at 1500 ºC for two reducing conditions are excluded for analysis), in which the 'continuous' δ profiles are straight line segments that connect these discrete δ points; (d) Arrhenius representation for extraction of thermodynamic properties by the van't Hoff method at selected fixed δ between 0.011 and 0.035. Comparison of the (e) standard enthalpy and (f) standard entropy of reduction of $YMnO_{3-\delta}$ determined using oxygen nonstoichiometry curves shown in Figure S3(a) and S3(c).